Modeling and Testing of an Improved HEMM Linear Motor

Aaron D. Anderson NASA Glenn Research Center Cleveland, Ohio, USA aaron.d.anderson-1@nasa.gov William R. Sixel

NASA Glenn Research Center

Cleveland, Ohio, USA

william.sixel@nasa.gov

Kirsten P. Duffy *University of Toledo* Toledo, Ohio, USA kirsten.p.duffy@nasa.gov Paul J. Passe HX5 LLC Brook Park, Ohio, USA paul.j.passe@nasa.gov

Abstract— Electrified aircraft propulsion systems require lightweight and highly efficient powertrain components including motors. Superconducting rotor coils can help enable such high-performance motors, but keeping the superconductors at the required cryogenic temperature is a challenge. NASA's 1.4 MW High Efficiency Megawatt Motor (HEMM) solves that problem by integrating a rotating pulse-tube cryocooler into the shaft. The cryocooler acoustic section is driven by a linear motor. This paper reports modeling, building, and testing a second version of that motor. Results reported here show significant improvements over the first version but also reveal remaining deficiencies.

Keywords—electric aircraft propulsion, linear motor, motor, cryocooler, superconducting motor

I. Introduction

NASA has been developing a 1.4 MW High Efficiency Megawatt Motor (HEMM) for the past several years [1] [2] [3] [4] [5] [6] [7] [8]. It uses a wound-field rotor with REBCO superconductor windings to generate a large rotating magnetic field with very low losses. A pulse-tube cryocooler, shown in Fig. 1, is integrated into the shaft and conductively cools the superconducting windings. The cryocooler piston is driven by a homopolar moving-magnet linear motor, the basic requirements of which are listed in Table I. Achieving an output movement range of 26% of the overall diameter creates significant challenges, both electromagnetically and mechanically. Design and testing of the first version of the motor is documented in [1]. This paper presents improvements on that design and further testing results. The electromagnetic design and validation are documented in II, dynamic testing and modeling in III, and conclusions in IV.



Fig. 1: Linear motor cross-section

Parameter	Requirement	
	Value	Unit
Outer diameter	≤100	mm
Output movement range	±13	mm
Peak output force	700	N
Operating frequency	56	Hz

TABLE I. LINEAR MOTOR REQUIREMENTS

II. ELECTROMAGNETIC DESIGN AND STATIC TESTING

Several issues with the electromagnetic design of the first version of the motor, V1, were discovered during testing. This section documents design changes for next version, V2, of the motor, detailed FEA modeling, and static testing of the V2 motor.

A. Design Changes

The first issue was that electromagnetic design of the V1 motor did not account for 3d effects of the outer iron segments, resulting in the iron saturating before generating the required output force. After detailed 3D FEA we decided to nearly double the axial thickness of the outer iron, ensuring that the peak flux density in the inner and outer iron are close to equal.

3D FEA further showed unacceptably high eddy current losses in the inner iron. Magnetic flux in the inner iron is primarily in the axial direction, so changes in flux induce circumferential eddy currents. Radial lamination of the iron would reduce eddy current losses but is not mechanically feasible, so instead radial slots are cut into the iron to approximate the effect of laminations, as shown in Fig. 2. The 24 radial slots in the V1 motor were not enough to reduce eddy current losses to an acceptable level for the thermal management system, so the number of radial slots was doubled for the V2 motor which brought the losses to an acceptable level.





Fig. 2: Inner iron V1 (left) and V2 (right), featuring twice as many radial slots.

This work was supported by the Advanced Air Transport Technology (AATT) project within NASA's Advanced Air Vehicles Program and the Aeronautics Research Mission Directorate.

In V1, the magnets were segmented into six segments, three sections circumferentially and two sections axially. 3D FEA predicted 155 W of eddy current losses in the magnets which was higher than acceptable. For V2, the magnets were divided into 24 total segments, with 12 circumferential sections and two axial sections, as shown in Fig. 3. This change resulted in modeled eddy current losses of only 1.9 W at full power. The small gaps between magnet segments required for assembly reduce the total amount of magnet material, which is mitigated by switching to a higher grade of samarium cobalt magnet resulting in nearly identical modeled output force generation.





Fig. 3: Magnet plunger V1 (left) and V2 (right), featuring more magnet segments.

B. FEA Results

A map of output force as a function of current across the full range of motion is shown in Fig. 4 with some cross-sections of the data shown in Fig. 5. In the first and third quadrants, the motor winding generates magnetic flux opposing the magnetization direction of the permanent magnets, so the total flux in the iron is relatively low. In the second and fourth quadrants, the magnetic flux from the winding is in the same direction as the permanent magnets resulting in larger flux density in the iron and ultimately saturation of the iron with sufficient current. This asymmetry means that at high-current operating points it takes less current to push the plunger away from center than to pull it back toward center, which will have an impact on dynamic performance at those operating points.

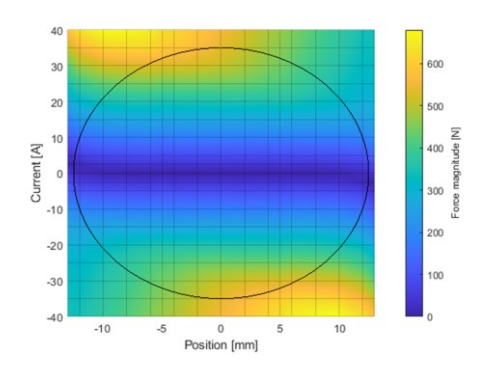


Fig. 4: Map of position, current, and force as modeled in FEA. The solid line indicates the operating points assuming resonant operation at peak output power and sinusoidal current and position waveforms.

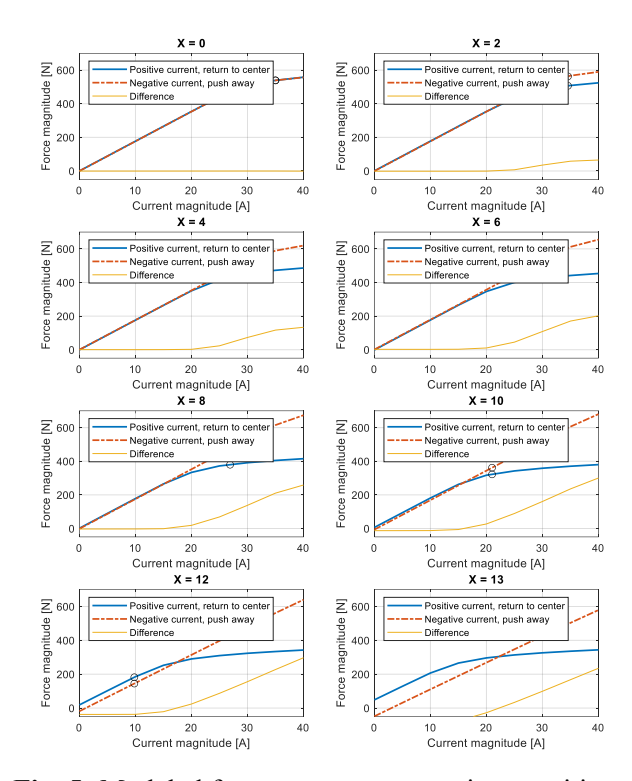


Fig. 5: Modeled force vs current at various positions.

C. Static Test Results

Fig. 6 shows the force generated by DC current with the magnet plunger fixed in the middle positions as modeled in FEA and as measured with a force transducer. At 40 A, the V2 motor generated only 54% as much force as modeled in FEA, which was far from the operational requirement. One possible reason for low output force would be larger than designed air gaps, or other issues with the magnetic circuit or coil. Measurement of the coil inductance was within a few percent of the modeled inductance, indicating that the problem was likely due to the magnet assembly not providing as much flux as designed.

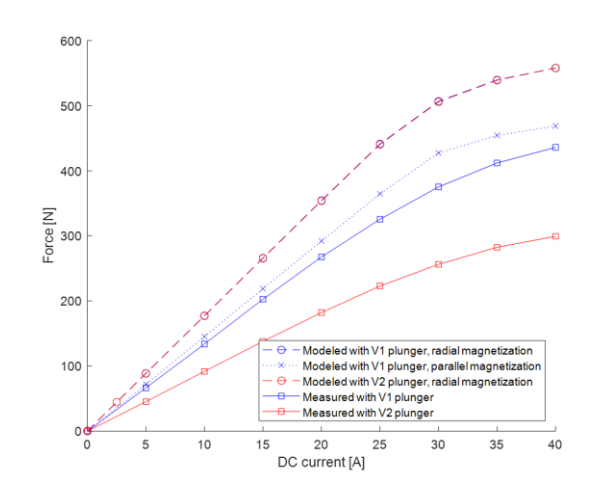


Fig. 6: Force vs DC current with plunger at center of travel.

To diagnose the performance of the magnet assembly, we disassembled the motor and rebuilt it with the magnet plunger from the V1 motor. In this condition, it generated 79% of the modeled force, a significant improvement but still not ideal. After disassembling the motor again, we directly measured the B-field generated by both magnet assemblies while sitting air.

The magnetic field distribution around the V1 plunger did not match very well with the modeled field distribution assuming radial magnetization as designed. However, as shown in Fig. 7, the fields matched much better when the magnets were modeled with each segment being magnetized with parallel fields rather than radial fields, as illustrated in Fig. 8. Unfortunately, parallel magnetization results in modeled output force 16% lower than with radial magnetization and about 7% higher than the measured force. The FEA model shows some self-demagnetization in the assembly, and the remaining difference between measured and modeled output force is likely due to additional demagnetization that occurred during assembly.

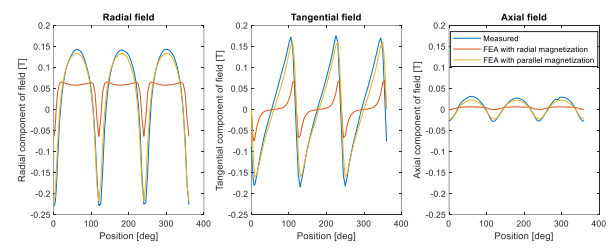


Fig. 7: Radial, tangential, and axial components of the magnetic field along the outside circumference of the V1 plunger 10 mm down from the axial end for both radial and parallel magnetization.

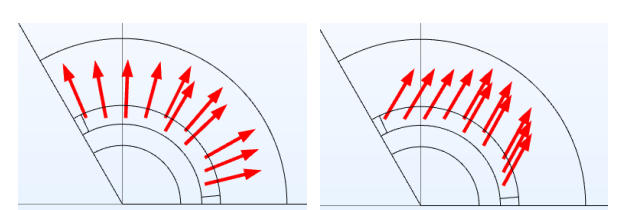


Fig. 8: Radial magnetization (left) vs parallel magnetization (right).

The measured field generated by the V2 magnet plunger are also consistent with each segment having approximately parallel magnetization rather than radial, though with more segments the difference is smaller. In addition, the measured fields are consistent with the magnets actually achieving only about half of the specified residual induction. These two factors explain much of the decreased output force generated. Unfortunately, during dynamic testing with the V2 magnet plunger, we experienced an incident where the plunger exceeded the maximum displacement and crashed into the stator breaking chunks off of several magnets. All field measurements were taken after this incident which makes quantitative assessment of the field difficult.

III. DYNAMIC OPERATION

After completing static testing, we moved on to unloaded dynamic testing using the V2 motor with the V1 magnet plunger.

This involved exciting the motor with a sinusoidal voltage source with no mechanical load attached to the output.

A. Resonant Operation

Our objective is to operate the motor at resonance, meaning that output force on the plunger and velocity of the plunger are in-phase [9]. During dynamic testing of the V1 motor we did not record the relative phases of voltage, current, and velocity or position and so could not accurately identify resonance. For the V2 motor, we switched from using a laser doppler vibrometer for velocity feedback to direct position sensing using a proximity probe sensing tapered target attached to the magnet plunger. We also improved the data acquisition to record relative phasing between voltage, current, and position. Since output force is proportional to the current in the coil, and position is by definition 90 degrees out of phase with velocity, we had enough information to detect resonance and adjust excitation voltage and frequency as needed.

Intuitively one might expect current and voltage to also be in-phase at resonance, but Fig. 9 shows that they are about 3 degrees out of phase due to the inductance of the coil. This phase angle will shift if there is a load force on the piston. Fig. 10 shows the phase angle between current and position as a function of frequency at various excitation voltages. Near resonance, the phase angle is very sensitive to small changes in voltage and frequency, which makes controlling the motor to operate at resonance tricky.

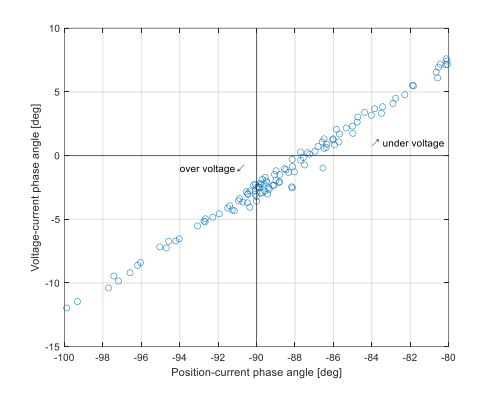


Fig. 9: Phase angle between current, position and voltage.

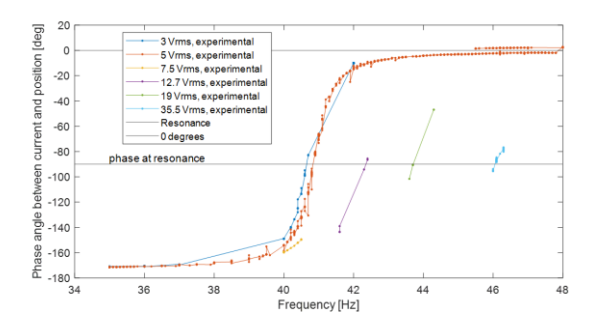


Fig. 10: Current-to-position phase angle as a function of frequency at various voltages.

As discussed in [1], the stiffness of the flexures has a cubic component, so we expect the resonant frequency to change depending on the magnitude of the displacement. Fig. 11 shows several performance characteristics as measured at resonance, as well as the theoretical resonance curve. However, the theoretical curve does not exactly match the observed behavior indicating that the parameters used to generate the theoretical curve are inaccurate or that there is some other nonlinear component in play.

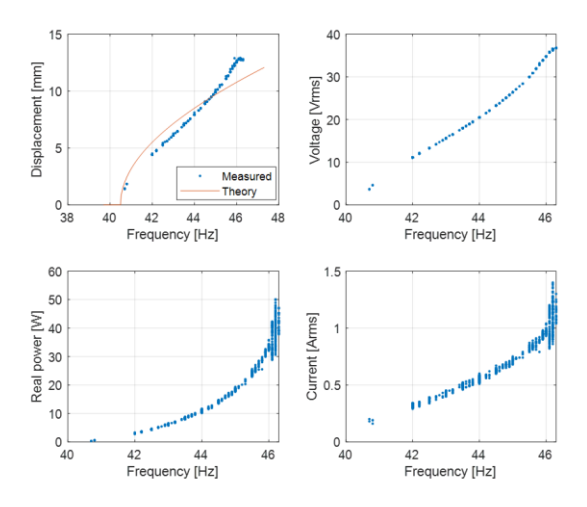


Fig. 11: Various performance metrics at resonance over a range of frequencies.

B. Off-Resonant Operation

Although most testing focused on resonant operation, we did run some off-resonance and can learn more about motor performance by looking at that data as well. Fig. 12 shows the relationship between frequency and displacement with various excitation voltages. At any given frequency, increasing voltage increases displacement, even when providing more voltage than is required for resonance. If excitation voltage is held constant, increasing the frequency from below resonance increases displacement until a critical, jump-down frequency above which the motor suddenly switches to a different regime and the displacement decreases dramatically, as observed in [1]. The motor continues operating in the lower displacement regime even as frequency is decreased until it hits the critical, jump-up frequency. Between the jump-down and jump-up frequency, the motor can operate stably in either regime. We directly observed the jump-up frequency for 5 V_{rms} operation, but reached displacement limits before observing the jump-down frequency at any voltage.

Fig. 13 is the current-position phase plane of this system with orbits of several different excitations plotted. The major axis of an orbit indicates the phase angle of that operating point. For example, at resonance the major axis is horizontal like the yellow and purple traces. Operating points with purely sinusoidal position and current will have smooth ellipses on the phase plane, while harmonics introduce complexity to the orbit. For example, Fig. 14 shows that there are significant harmonics in the position and slight harmonics in the current waveform for the orbit shown in green.

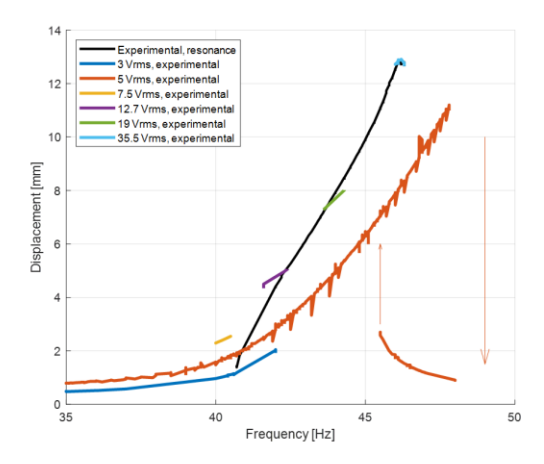


Fig. 12: Displacement vs frequency at various voltages.

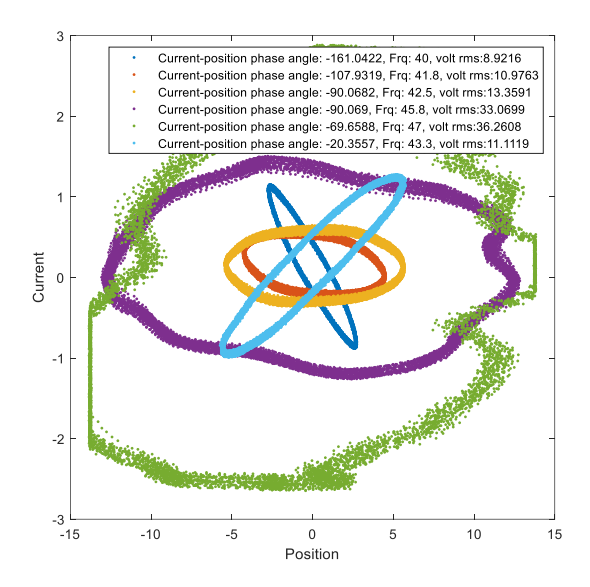


Fig. 13: Current vs position at various operating conditions.

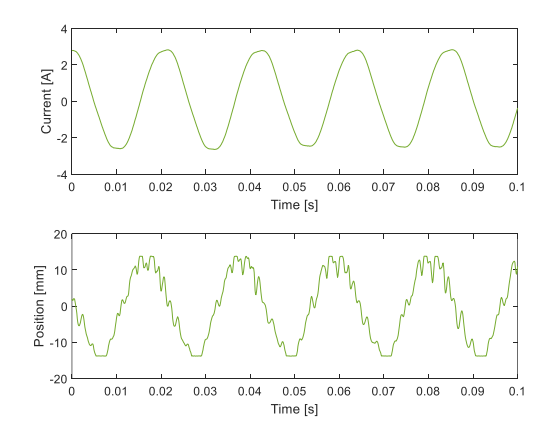
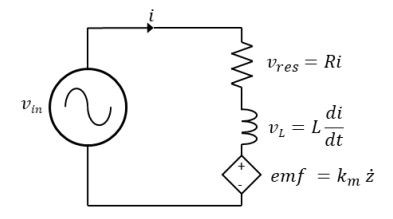


Fig. 14: Time dependent current and position for the $11 V_{rms}$, 43.3 Hz operating point.

C. Numerical Modeling of Dynamic Performance

In addition to collecting experimental performance data, we also developed a model of the motor which can be solved numerically to allow for further investigation of dynamic performance. Fig. 15 shows block diagrams and governing equations that describe the system. Electrical parameters of the system are the resistance, inductance, and back-emf constant, while the mechanical parameters are mass, damping ratio, and spring constants. The back-emf constant is actually a non-linear fit based on measured force vs current and expanded using the FEA model. All other input parameters set to measured values where possible and FEA predictions where not possible.



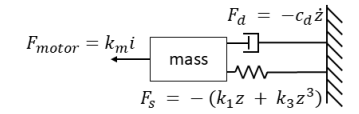
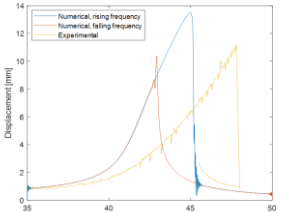


Fig. 15: Block diagrams and governing equations for numerical modeling.

The displacement magnitude with fixed 5 V excitation and a sweep of frequencies is shown in Fig. 16. The general shape of this response is similar to the measured performance, including exhibiting both operating regimens mentioned in section III.B. However, the modeled displacement deviates appreciably from the experimental results indicating that some or all of the model parameters do not match or there are additional parameters not captured in the model.



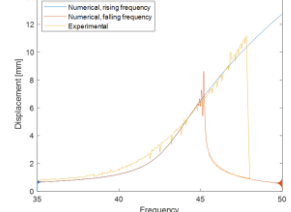


Fig. 16: Modeled and experimental displacement vs frequency with 5 V_{rms} excitation, original parameters on the left, updated parameters on the right.

To determine likely sources of the discrepancies, we ran the numerical model repeatedly while varying each input parameter. This showed that performance is highly sensitive to changes in k_1 and mass, and small changes to the other parameters have smaller impacts on overall performance. After some trial and error, we found that the model matched the measured performance better with k_1 increased by 10%, k_3 increased by a factor of 2.6, and c_d decreased by 20%. The response at 5 V

excitation with these adjusted parameters is also shown in Fig. 16. Sweeps over a broader range of frequencies and voltages are shown in Fig. 17, and the corresponding phase plot of phases is in Fig. 18.

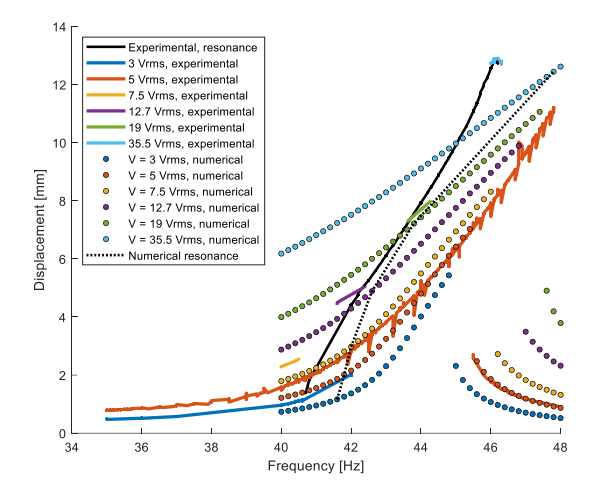


Fig. 17: Numerically modeled and experimentally measured displacement vs frequency at various excitation voltages.

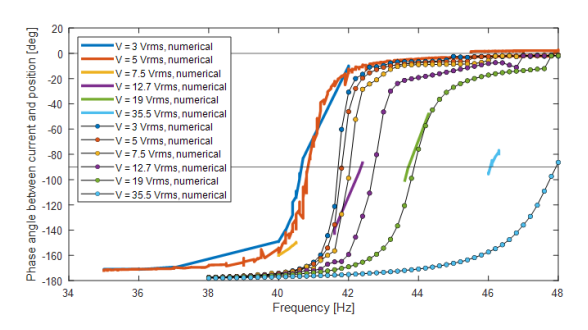


Fig. 18: Numerically modeled and experimentally measured phase angle vs frequency at various excitation voltages.

Clearly, this model does not fully capture the characteristics of the motor but it is close enough to provide some utility for understanding performance at a variety of operating points. Future refinements of the numerical model may include adding electromagnetic loss sources present like iron losses, eddy current losses on the magnets, and proximity losses in the coil.

IV. CONCLUSIONS AND FUTURE WORKS

The V2 linear motor for the HEMM cryocooler performed significantly better than the V1 motor despite some setbacks along the way. FEA modeling revealed areas of high loss and design changes were made to reduce those losses. Modeling also showed severe saturation of the iron and the geometry was adjusted to reduce the impact of saturation. With these changes implemented, stationary testing showed lower than expected force generation. The root cause was determined to be parallel rather than radial magnetization of the magnet plunger as well as incomplete magnetization.

During dynamic testing, accurate position sensing and recording of phase data allowed for reliable operate at resonance as well as mapping performance at non-resonant operating points. Numerical modeling of the motor showed that cubic stiffness alone does not explain the nonlinear resonant behavior of the system so further refinement of the model could provide more insight.

REFERENCES

- [1] K. P. Duffy, P. J. Passe, R. W. Dyson, R. H. Jansen, Y. D. Jesus-Arce and A. D. Anderson, "Design, Analysis, and Testing of the HEMM Cryocooler Linear Motor," in 2020 AIAA/IEEE Electric Aircraft Technologies Symposium (EATS), New Orleans, LA, USA, 2020.
- [2] G. Szpak, A. Smith, J. T. Thompson, A. Woodworth and R. Jansen, "High Efficiency Megawatt Motor Thermal Stator Preliminary Design," in AIAA/IEEE Electrified Aircraft Technologies Symposium, New Orleans, LA, USA, 2020.
- [3] R. H. Jansen, P. Kascak, R. Dyson, A. Woodworth, J. Scheidler, A. D. Smith, E. Stalcup, T. Tallerico, Y. d. Jesus-Arce, D. Avanesian, K. Duffy, P. Passe and G. Szpak, "High Efficiency Megawatt Motor Preliminary Design," in 2019 AIAA/IEEE Electric Aircraft Technologies Symposium (EATS), Indianapolis, IN, USA, 2019.
- [4] R. H. Jansen, J. Scheidler, T. Tallerico, P. Kascak, A. Woodworth, A. Smith, R. Dyson, W. Sixel, J. Thompson,

- E. Stalcup, Y. D. Jesus-Acre, D. Avanesian, K. Duffy, P. Passe and G. Szpak, "High Efficiency Megawatt Motor Risk Reduction Activities," in *AIAA/IEEE Electrified Aircraft Technologies Symposium*, New Orleans, LA, USA, 2020.
- [5] R. W. Dyson, R. H. Jansen, K. P. Duffy and P. J. Passe, "High Efficiency Megawatt Machine Rotating Cryocooler Conceptual Design," in *AIAA Propulsion and Energy Forum*, Indianapolis, IN, USA, 2019.
- [6] R. H. Jansen, Y. D. Jesus-Arce, D. P. Kascak, D. R. Dyson, D. A. Woodworth, D. J. Scheidler, R. Edwards, E. Stalcup and J. Wilhite, "High Efficiency Megawatt Motor Conceptual Design," in 2018 Propulsion and Energy Forum and Exposition, Cincinnati, OH, USA, 2018.
- [7] J. J. Scheidler, "Preliminary Design of the Superconducting Rotor for NASA's High-Efficiency Megawatt Motor," in AIAA Propulsion and Energy Forum, Cincinnati, OH, USA, 2018.
- [8] T. Tallerico, J. J. Scheidler, D. Lee and K. S. Haran, "Electromagnetic Redesign of NASA's High Efficiency Megawatt Motor," in 2020 AIAA/IEEE Electric Aircraft Technologies Symposium, Virtual, 2020.
- [9] G. W. Swift, Thermoacoustics: A unifying perspective for some engines and refrigerators, Springer, 2017.